

Molecular Mechanism of Brassinosteroid Perception by the Plant Growth Receptor BRI1

Faisal Aldukhi,^{†,○} Aniket Deb,^{#,○} Chuankai Zhao,^{†,●} Alexander S. Moffett,^{‡,●} and Diwakar Shukla^{*,†,‡,§,||,⊥,▽,●}

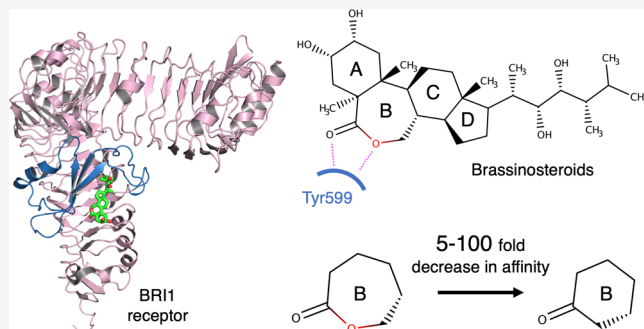
[†]Department of Chemical and Biomolecular Engineering, [‡]Center for Biophysics and Quantitative Biology, [§]Department of Plant Biology, ^{||}NIH Center for Macromolecular Modeling and Bioinformatics, and [⊥]Beckman Institute for Advanced Science and Technology, University of Illinois at Urbana-Champaign, Urbana, Illinois 61801, United States

[#]Department of Food Technology and Biochemical Engineering, Jadavpur University, Kolkata, West Bengal 700032, India

[▽]National Center for Supercomputing Applications, Urbana, Illinois 61801, United States

S Supporting Information

ABSTRACT: Brassinosteroids (BRs) are essential phytohormones, which bind to the plant receptor, BRI1, to regulate various physiological processes. The molecular mechanism of the perception of BRs by the ectodomain of BRI1 remains not fully understood. It also remains elusive why a substantial difference in biological activity exists between the BRs. In this work, we study the binding mechanisms of the two most bioactive BRs, brassinolide (BLD) and castasterone (CAT), using molecular dynamics simulations. We report free-energy landscapes of the binding processes of both ligands, as well as detailed ligand binding pathways. Our results suggest that CAT has a lower binding affinity compared to BLD due to its inability to form hydrogen-bonding interactions with a tyrosine residue in the island domain of BRI1. We uncover a conserved nonproductive binding state for both BLD and CAT, which is more stable for CAT and may further contribute to the bioactivity difference. Finally, we validate past observations about the conformational restructuring and ordering of the island domain upon BLD binding. Overall, this study provides new insights into the fundamental mechanism of the perception of the two most bioactive BRs, which may create new avenues for genetic and agrochemical control of their signaling cascade.



INTRODUCTION

Plants, being immobile, face considerable challenges in adapting to their changing environments to grow and survive.¹ Environmental signals, such as temperature and light, must then be sensed and acted upon by the plant intracellular system.² This process of generating cellular responses to external environmental stimuli is facilitated via phytohormones. Brassinosteroids (BRs) represent an important category of phytohormones, which influence a wide range of physiological processes critical for plant growth and development.³ Mutants with defects in the biosynthesis or signaling of BRs show multiple inadequacies such as dwarfism, delay in flowering, reduced germination of seeds, low fertility levels, and improper stomatal distribution.⁴ BR signaling starts with the brassinosteroid insensitive 1 (BRI1), a receptor kinase present at the cell surface. The extracellular domain of BRI1 recognizes BRs, which leads to heteromerization with the coreceptor BRI1-associated receptor kinase1 (BAK1), a member of the somatic embryogenesis receptor kinase (SERK) family of proteins. This is followed by the transphosphorylation of the intracellular kinase domains of BRI1 and BAK1, which triggers a downstream signaling cascade

eventually leading to the expression or suppression of important genes.^{1,4–7}

The perception of BRs by the BRI1 receptor is a crucial step in the BR signaling pathway.⁸ Previous studies have provided insights into the structure of this important plant receptor.^{9–12} BRI1 is localized in the plant cell membrane and consists of an extracellular ligand binding domain, a single transmembrane helix, and an intracellular kinase domain with serine/threonine specificity. The extracellular domain consists of 25 leucine-rich repeats (LRRs) and assumes a right-handed superhelical structure (Figure 1).^{9,11} A notable feature of this part of the receptor is the presence of an island domain, which consists of 70 amino acid residues between the LRRs 21 and 22.^{9,12} The crystal structure of BRI1 with brassinolide (BLD), the most active BR (Figure 1A), bound reveals that LRRs 21–25 along with the island domain form the binding pocket for BLD.^{9,12} It was suggested that BLD binding does not induce much conformational change in the LRR core of BRI1.^{9,12} However,

Received: October 4, 2019

Revised: December 23, 2019

Published: December 24, 2019

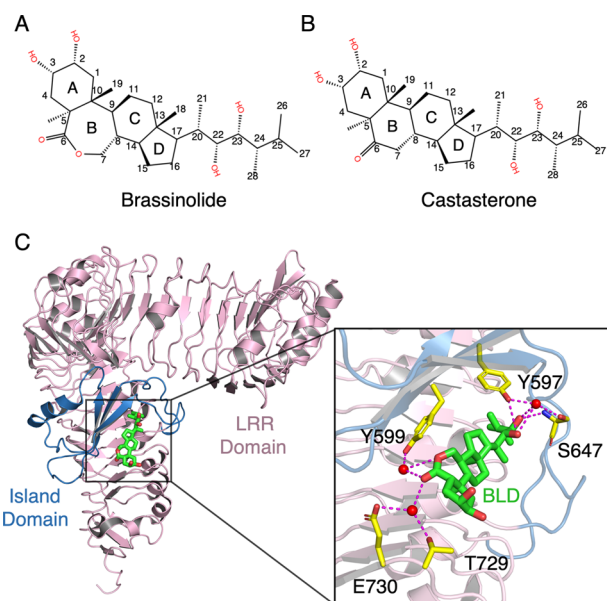


Figure 1. Chemical structures of (A) BLD and (B) CAT. The difference between the two molecules is the extra oxygen in the B-ring of BLD. (C) Crystal structure of the BRI1–BLD complex (PDB ID: 3RGZ). The LRR core of the receptor is shown in pink and the island domain in sky blue. BLD is shown as green sticks, while water molecules are shown as red spheres. Hydrogen bonds (magenta), either direct or water-mediated, between BLD and the residues of the island domain and LRR core of BRI1 are shown in the enlarged view.

the island domain becomes increasingly ordered upon the binding of BLD, allowing for the activation of the receptor.^{9,12} When BLD is bound to BRI1, the A–D rings of BLD are positioned in a hydrophobic groove between the LRR core and the island domain, while its alkyl chain goes into a small pocket formed by LRRs 21 and 22 and the island domain (Figure 1C). Interactions of BLD with the residues of the island domain and LRR core appear to be essential for BLD binding. Mutations in the residues of the island domain, as well as of the nearby LRRs, have been reported to adversely affect BLD binding and consequently the downstream signaling.^{8,9,12,13} Thus, the island domain and the surrounding LRR core are indispensable for BLD perception.

Within the family of naturally synthesized BRs, BLD and castasterone (CAT, Figure 1B) are the most widely distributed in plants.¹⁴ In *Arabidopsis thaliana*, they have been isolated in the shoots, seeds, and root calluses. BLD is isolated at higher quantities in the root callus, while CAT is the dominant BR in the shoots.¹⁵ Previous results have classified BLD as the most bioactive BR.¹⁶ It is structurally a steroid with a unique lactone group in its B-ring and vicinal diols in both its A-ring and alkyl chain (Figure 1A).¹⁷ CAT is the second most potent BR and the immediate precursor of BLD in BR biosynthesis.^{16,18} It is structurally almost identical to BLD with the only difference being the absence of an oxygen atom between C6 and C7 carbons in the B-ring (Figure 1B).¹⁹ Although CAT can also act as a biologically active BR, it has been reported to be much less active than BLD, with difference ranging from 5-fold in rice lamina inclination test,^{20,21} 10-fold in the mung bean explant test²² to a 100-fold in the pinto-bean second internode test.²³ It remains unclear how these two hormones with strikingly similar structures can have such a considerable difference in their biological activity.

Despite advances in the mechanistic understanding of BR signaling, a large number of questions remain unanswered regarding the perception of BRs. The structural characterization of BRI1 via crystallographic methods has given crucial insights into the mode of action of BLD. However, a detailed atomic view and quantitative thermodynamic and kinetic characterizations of the binding of BLD to BRI1 are still lacking. Furthermore, there is limited information about the binding mechanisms of BRs other than BLD such as CAT. Particularly, the binding pose for CAT remains to be characterized. Biochemical assays have provided significant information about the relative differences in the biological activities of BRs. However, the molecular origin of the activity differences between BLD and CAT remains unclear. Therefore, a complete dynamic view and a detailed thermodynamic and kinetic investigation on the binding processes of BRs are required to fully understand their perception mechanism.

To answer these vital questions, one requires a tool that can describe the receptor conformations and interactions with the ligands at a high spatial–temporal resolution. Molecular dynamics (MD) simulations have gained considerable popularity as a tool for studying the dynamic behavior of biological systems at the atomic level.^{24–28} However, MD simulations alone typically require significant computational time to fully characterize long time scale biological processes, such as ligand binding, which occur in microseconds to milliseconds. One way to counter this is to combine MD simulations with adaptive sampling and Markov state models (MSMs).^{29–32} This computational framework allows us to efficiently sample rare biological events and construct a discretized kinetic network model to describe the thermodynamics and kinetics of biological processes.^{33–35} This approach of MD simulations followed by MSM analysis has previously been successful in predicting protein–ligand binding processes^{36,37} and elucidating important conformational changes in proteins.^{38–41}

In this study, we employed the combined approach of MD simulations and MSM analysis to answer important questions regarding the perception of BLD and CAT by BRI1 in *A. thaliana*. We have performed ~58 and ~44 μ s MD simulations to capture the binding of BLD and CAT to BRI1, respectively. We report free-energy landscapes to describe the thermodynamics of the binding of both ligands and identify the important binding intermediate states. We have replicated the bound pose for BLD including the important interactions with BRI1 residues as elaborated by the crystal structures. We have also predicted the previously unknown bound pose for CAT. We have illustrated the binding pathways for both ligands, detailing which residues interact with the ligands at each step. Our results suggest that CAT cannot form critical polar interactions with a tyrosine residue present in the island domain of BRI1, resulting in a lower binding affinity compared to BLD. The attenuated interaction with BRI1 for CAT is due to the absence of an oxygen atom in the B-ring, which is suggested by our long time scale kinetic Monte Carlo simulations. In addition, we uncover a conserved non-productive binding state for both BLD and CAT, which can potentially decrease the ligand affinity by affecting their on-binding rates. Furthermore, the nonproductive pose is more stable for CAT, which may contribute to the difference in bioactivity between BLD and CAT. Finally, we have validated previous studies that illustrate a conformational restructuring of the island domain post ligand binding. Overall, our findings improve the understanding of BR perception, which allows for

future chemical and genetic control of BRI1 receptor activity and the associated biological responses.

■ THEORETICAL METHODS

MD Simulations and Adaptive Sampling of Ligand Binding to BRI1. In essence, MD simulations illustrate the motions of the atoms in a simulation system with respect to time.²⁸ If the spatial positions of all of the atoms at a particular point of time and the net force on each atom acted by the other atoms of the system are known, Newton's second law is applied to predict the future positions of the atoms.²⁷ The MD simulations for both our ligand systems were conducted using the crystal structure of BLD-bound BRI1 as the initial structure (PDB ID: 3RGZ⁹). To save computational time, the N-terminal residues 29–322 of the receptor protein were truncated in VMD,⁴² resulting in a structure containing residues 323–741 used for our MD simulations. We believed that the truncated region would have no impact on ligand binding to BRI1, given that the BRI1 crystal structures without and with BLD-bound are nearly identical and the truncated region is far away from the binding site.⁹ The truncated BRI1 structure was then capped at the N-terminal with ACE and at the C-terminal with NME. PDBFixer was used to add the missing atoms and hydrogens.⁴³ The protonation states of the histidine residues were inspected using the H++ server at pH of 7.⁴⁴ The force field used for the protein was AMBER ff14SB⁴⁵ and that for the ligands was the general AMBER force field.⁴⁶ The partial charges for the ligands were derived using antechamber in Ambertools15 according to the AM1-BCC method.⁴⁷ The disulfide bonds formed by the cysteine residues were added where necessary using tleap. To neutralize the system and imitate the conditions of the living cells, 150 mM of sodium chloride was added to the system. The ligands were initially placed randomly at multiple positions, with the distances at least 15 Å, away from the BRI1 binding site. For BLD, the system contained 52809 atoms in total, with a periodic cell size of $108.6 \times 76.9 \times 63 \text{ Å}^3$. For CAT, the system included 54 500 atoms with a periodic cell size of $109.1 \times 77.3 \times 64.4 \text{ Å}^3$.

Both the systems were minimized for 50 000 steps and then equilibrated for 10 ns. Production simulations were launched from the equilibrated structures and performed at isothermal–isobaric ensemble (300 K, 1 atm) using an integration time step of 2 fs. The temperature was controlled using Langevin dynamics⁴⁸ with a collision frequency of 2 ps^{-1} , and the pressure was maintained using Berendsen barostat⁴⁹ with a relaxation time of 1 ps. Periodic boundary condition was applied in all MD simulations. The particle-mesh Ewald method was used to treat the electrostatic interactions, along with a 10 Å cutoff distance for van der Waals interactions.⁵⁰ The SHAKE algorithm⁵¹ was applied to constrain the length of covalent bonds involving hydrogen atoms. To capture the long time scale process of ligand binding efficiently in a relatively short amount of simulation time, the strategy of adaptive sampling was employed.^{29–32} Previous studies have successfully utilized the adaptive sampling approach to study protein–ligand binding processes.^{36,52,53} The simulation procedure for performing adaptive sampling simulations consists of iteratively running short parallel simulations and seeding new simulations from configurations chosen based on the currently sampled conformations. In the first round of simulations, the ligands were randomly positioned at multiple positions outside of the binding site of the BRI1 receptor, with the distances of at least

15 Å away. In the next round of simulations, the starting configurations were chosen from the simulation snapshots, which have the ligand at the minimum distance from the binding pocket. The simulations were stopped when we have observed ligand binding and obtained sufficient simulation data to build a Markov state model of the ligand binding process. In this way, we directed our simulations to sample toward the protein–ligand-bound states, which led to enhanced computational efficiency. All of the simulations were run in AMBER14 (for BLD) and AMBER18 (for CAT).⁴⁷ The simulations were conducted using either a local cluster or the Blue Waters supercomputer.⁵⁴ The total simulation time was 58 μs for BLD binding and 44 μs for CAT binding (Tables S1 and S2).

Markov State Model Construction and Hyperparameter Selection. MSMs are powerful analytical tools to analyze a large amount of MD simulation data on biomolecule, allowing for a rigorous statistical analysis of rare biological events.^{33–35} The MSMs combine all short parallel trajectories and discretize sampled biomolecule conformational space into a kinetic conformational network model, where the nodes represent a certain number of kinetically relevant conformational states and the edges represent transition probabilities between these states.^{33–38,55} Using MSMs, we can predict the long time scale dynamics of biomolecule that are far beyond the time scales of single short trajectories.^{33–35} We constructed MSMs to analyze our protein–ligand binding simulation datasets, which were then used to determine equilibrium probabilities of conformational states, thermodynamics, and kinetics of ligand binding, as well as protein–ligand binding pathways. Previous studies have demonstrated using the adaptive sampling and MSM approach to study protein–ligand binding processes.^{36,52,53}

To generate an MSM, a selection of features relevant to the system was made. For our ligand–protein systems, these were distance metrics, which could accurately describe the movement of the ligands during the binding processes. A set of distances between the atom pairs belonging to BRI1 and both ligands were chosen as the features (Tables S3 and S4). The first subset of features were pairwise distances between the C_α atoms of the residues within 5 Å of the bound ligands and three atoms in the ligands. The rest of the distance features were specific interactions between BRI1 and the bound ligands. Featurization of the simulation datasets was performed using MDTraj 1.7.0.⁵⁶

Dimensionality reduction was then performed for clustering the conformation ensemble from MD simulations into kinetically relevant states. This was implemented using time-lagged independent component analysis (tICA), an approach to analyzing the slower dynamics of protein systems.⁵⁷ tICA was performed on the normalized featurization dataset to generate the slowest relaxing degrees of freedom from the linear combinations of the features. Next, the data for each ligand system, representing all of the conformations generated from MD simulations, was clustered into a number of states based on several tICs using the *k*-means clustering method. A number of MSMs were then built using the clustering result with different lag times. The lag times, at which the slowest implied time scales captured by these MSMs converge, were chosen for building MSMs (Figure S1). The numbers of clusters and tICs for both systems were further optimized through a cross-validation method, which used the generalized matrix Rayleigh quotient (GMRQ) score to estimate the slow

dynamic modes of the protein systems.⁵⁸ The numbers of tICs and clusters, which corresponded to the highest GMRQ scores for each system, were chosen as the optimum ones to build the MSMs (Figure S2). tICA, clustering, and MSM construction were implemented using the MSMBuilder 3.4 python package.⁵⁹ The iteration processes to estimate GMRQ scores for MSMs were performed using Osprey, which is a tool for hyperparameter optimization of machine learning algorithms.⁶⁰ The graphs were plotted using the Matplotlib 3.1.1 python package.⁶¹ The final MSM parameters for BLD were 200 clusters, 6 tICs, and a lag time of 20 ns and those for CAT were 80 clusters, 3 tICs, and a lag time of 20 ns.

Estimation of Standard Binding Free Energy from Potential of Mean Force. The standard binding free energies (ΔG°) for both BLD and CAT to BRI1 were estimated from the three-dimensional potential of mean force $W(r)$ (3D PMF).^{52,62} The 3D PMFs were generated by projecting the relative positions of both ligands to BRI1 onto the Euclidean coordinates, weighted by their equilibrium probabilities given by the MSMs (Figures S3 and S4). ΔG° was then calculated using the following expression

$$\Delta G^\circ = -\Delta W_{3D} - k_B T \log\left(\frac{V_b}{V^\circ}\right) \quad (1)$$

where ΔW_{3D} is the depth of the 3D PMF, k_B is the Boltzmann constant, T is the temperature, V_b is the bound volume calculated as the integral of the PMF, and V° is the standard-state volume, which is 1661 \AA^3 . V_b is given by

$$V_b = \int_b \exp(-\beta W(r)) dr \quad (2)$$

where the bound region is defined by a cutoff distance from the minima of the 3D PMF and a cutoff $W(r)$. A sensitivity analysis was performed to choose the appropriate cutoff distance and $W(r)$ to define the bound volume.⁵²

Kinetic MC Simulations of Ligand Binding Dynamics.

The binding kinetics of the ligands over long time scales can be estimated by running kinetic Monte Carlo (MC) simulations on the MSMs. This is essentially a probabilistic approach, which relies on the MSM transition probability matrix to sample the protein–ligand conformational space and generate artificially long trajectories. Analysis of these trajectories can give kinetically relevant information about important rare biological events captured by the MSMs, such as ligand binding in our study.⁶³ For both our systems, the starting states were chosen such that the ligands were more than 40 Å away from the receptor. The kinetic MC trajectories were generated using the MSMBuilder 3.4 python package.⁵⁹

To quantitatively characterize the time scale of ligand binding and unbinding, we estimated the on-binding and off-binding rate constants (k_{on} and k_{off}) using the following formulas⁵²

$$k_{on}^{-1} = \text{MFPT}_{on} \times C^{\text{comp}} \quad (3)$$

$$k_{off}^{-1} = \text{MFPT}_{off} \quad (4)$$

where MFPT_{on} and MFPT_{off} are the mean first passage time to the bound and unbound states, and C^{comp} is the ligand concentration in the simulation box. The unbound states were chosen such that the ligands were more than 30 Å away from the receptor. The bound states were chosen such that the RMSDs of the ligands were less than 2 Å as compared to their

respective bound poses and also their distances from S647, an important residue interacting with both ligands in their bound poses, were less than 4 Å.

Transition Path Theory (TPT) Analysis of Ligand Binding Processes. Transition path theory (TPT) serves as a tool to calculate the probabilities and fluxes for the pathways between the source and sink states in MSMs.^{64,65} TPT can be applied in the context of our protein–ligand problems to generate the most probable pathways via which the ligands can reach their final bound states starting from initially unbound states. The ligand-unbound states and the bound states were chosen using the same metrics as described above. Essentially, given the ligand-unbound states and the ligand-bound states as the source and the sink states for TPT analysis, we were able to obtain numerous pathways that connected through the unbound and the bound states, which corresponded to the ligand binding pathways. By comparing the fluxes of these pathways, we identified the top favorable binding pathways for both BLD and CAT. The transition pathways were estimated using the MSMBuilder 3.4 python package.⁵⁹

Root-Mean-Square Fluctuation (RMSF) Analysis of the Island Domain. The flexibility of the protein backbone can be captured by calculating the root-mean-square fluctuation (RMSF) of the C_α atoms of the residues in BRI1. RMSF is a measure of atomic fluctuations and can be an effective tool to compare differences in protein conformation before and after ligand binding. For both our systems, the RMSF values were generated after superimposing each frame of the trajectories against the conformation of BRI1 bound with BLD. The RMSF calculations were carried out using the PyTraj 2.0.1 python package.⁶⁶

RESULTS AND DISCUSSION

Thermodynamic Analysis of Ligand Binding Processes Reveals a Higher Affinity for BLD Than That for CAT and Key Binding Intermediate States. Using extensive adaptive MD simulations, we obtained the binding of both BLD and CAT to the BRI1 receptor starting from the states where the ligands were far away from the binding site. There were 58 out of 1000 trajectories for BLD and 143 out of 737 trajectories for CAT that successfully captured the partial binding events (i.e., starting from where the RMSD of the ligand from the bound pose was more than 8 Å and reaching the binding site in the end). To gain thermodynamic insights into the ligand binding processes, we estimated the standard binding free energy (ΔG°) for both ligands and generated the free-energy landscapes that provided the energetic description of the processes. The three-dimensional PMFs along the Euclidean coordinates were produced to estimate the depth of PMF ΔW_{3D} for BLD and CAT, which are 15.01 ± 0.12 and 11.02 ± 0.1 kcal/mol, respectively (Figures S3A–C and S4A–C). We varied the cutoff distance and the cutoff $W(r)$ to define V_b and then characterized the changes in V_b and ΔG° (Figures S3D,E and S4D,E). After the sensitivity analysis, we defined the bound conformation as those states with a distance of less than 10 Å from the 3D PMF minima and $W(r)$ less than 2 kcal/mol. The 3D PMFs yielded a standard free energy of binding $\Delta G^\circ = -10.77 \pm 0.11$ kcal/mol for BLD and $\Delta G^\circ = -6.9 \pm 0.11$ kcal/mol for CAT. The error bars on ΔG° were determined by averaging over 10 PMFs by the projection of random 50% of simulation data, weighted by their equilibrium probabilities generated from Bayesian MSMs. Our predicted ΔG° for BLD is in good agreement with the experimental

$\Delta G^\circ_{\text{exp}} = -10.92 \text{ kcal/mol}$.⁶⁷ The lower ΔG° for BLD binding suggests that BLD has a higher binding affinity as compared to CAT. This is also in accordance with the previous studies reporting that BLD is the most potent BR.^{20–23}

To quantitatively characterize the ligand binding processes, we generated the free-energy landscapes by projecting the conformations onto two important structural metrics instead of the Euclidean coordinates (Figure 2A,B). For each system, the

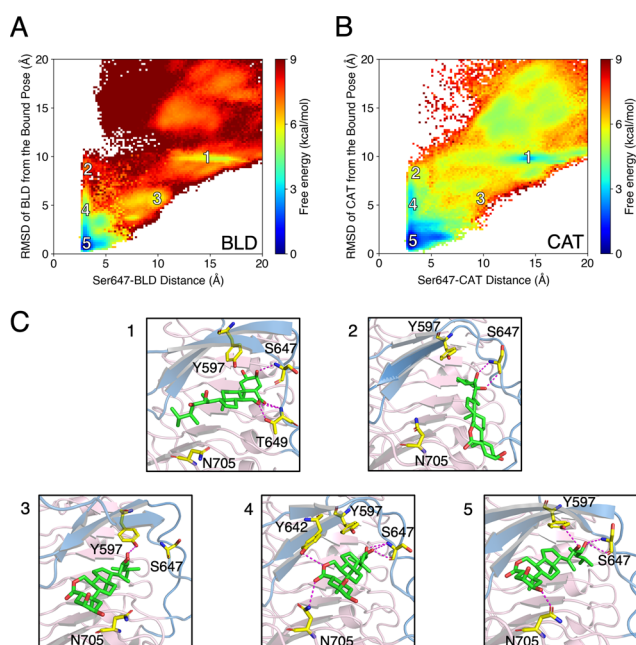


Figure 2. Free-energy landscapes for both (A) BLD binding and (B) CAT binding to BRI1 are constructed by projecting all of the simulated conformations, weighted by the MSMs, in the context of two metrics including the distance of the ligands from S647 and the RMSD of the ligands from their bound poses. (C) Conformations of the ligand–protein system for BLD corresponding to the state labels in the free-energy landscape are shown. The LRR core of BRI1 is shown in light pink and the island domain in sky blue. BLD is shown as green sticks while the important residues of BRI1, involved in direct hydrogen bonding with BLD, are shown as magenta sticks.

distance of the ligand from S647 of BRI1 and the RMSD of the ligand from its bound pose were selected as the two structural metrics. The distance from S647 was chosen as this BRI1 residue was observed to interact with the ligands in several intermediate states, as well as in their bound states. The RMSD of the ligands from their bound pose was chosen as it accurately reflects the deviation of the ligands from their final bound pose. We also estimated the error bars on the binding free-energy landscapes (Figure S5).

A deeper analysis of the free-energy landscapes revealed the key conformational states during the binding processes (marked as states 1–5 in Figure 2A,B). The snapshots corresponding to these states for BLD binding are shown in Figure 2C. States 1–4 are key intermediate states, while state 5 represents the ligand-bound configuration of the receptor. In state 1, the rings A–D of BLD are positioned inside the small binding pocket formed by LRRs 21 and 22 and the island domain. In this position, the hydroxyl group of C2 of the A-ring interacts with S647, while the oxygens of the B-ring interact with T649. This conformation is flipped with respect to the final bound pose, where the hormone side chain resides

in the small binding pocket instead of the fused rings. We thus propose that this might be a nonproductive binding pose attained by BLD during binding. This nonproductive binding is also captured in the CAT binding process (Figure 2B). These states potentially reduce the affinity of BRs by lowering the on-binding rates. On the other hand, in the intermediate state 4, BLD has assumed the orientation in the bound pose but is yet to fix itself in the correct configuration. It interacts with S647 via the vicinal diols of its side chain, with Y642 via the ring oxygen of its B-ring and N705 via the carbonyl oxygen of its B-ring. The positions of the two intermediate states in the free-energy landscape indicate that BLD may be able to bind to BRI1 via more than one pathway.

To better show the two different pathways BLD might follow, we characterized states 2 and 3, which appear to precede state 4 and succeed state 1, respectively. State 2 describes a configuration where the BLD side chain appears to approach the binding pocket. The side-chain vicinal diols form hydrogen-bonding interactions with S647. State 3 corresponds to a configuration where the BLD side chain is oriented to enter the binding pocket but has not done so yet. In this state, BLD forms a hydrogen-bonding interaction with the Y597 via the hydroxyl group attached to C23 in its side chain. It is observed from the free-energy landscape that there is a considerable energy barrier ($\sim 4 \text{ kcal/mol}$) between state 1 and state 3. To reach from states 1 to 3, the linked rings in BLD have to move out of the binding pocket and reverse its orientation to allow the side chain to enter the binding pocket instead. The enhanced stability of the nonproductive binding pose described by state 1 may be the reason for such an energy barrier associated with the flipping process. In contrast, the transition from state 2 to state 4 and finally to the bound state 5 faces no significant energy barrier, with the landscape showing a gradual decrease in free energy.

In addition, there is a distinct similarity between the BLD and CAT landscapes in terms of the landscape shapes and the positions of the energy minima. Consequently, the intermediate states for the binding of each ligand are also observed to be similar to the degree allowed by their structural difference. An important difference, however, in the case of CAT is the lower free energy associated with the nonproductive binding state 1 as compared to BLD ($\sim 3 \text{ kcal/mol}$ difference). As a result, it is possible that CAT may spend more time in this pose at equilibrium, thus hindering the flipping process to assume the bound pose. This could be another reason for the lower biological potency of CAT. Overall, our thermodynamic results have revealed several key states during ligand binding for both systems and have also provided energetic insights into why BLD is more bioactive than CAT.

Simulations Unveil the Previously Unknown Bound Pose for CAT. MD simulations and consequent MSM analysis have captured the bound poses for both BLD and CAT. The pose captured for BLD is identical to that of the crystal structure (Figure 3A) (PDB ID: 3RGZ⁹), with the RMSD of the simulated bound pose less than 1 Å from the crystal structure. We have accurately reproduced several of the BRI1–BLD interactions as well (Figure 3B).^{9,12} The BRI1 residues involved in BLD perception are S647, Y597, Y599, and H645 of the island domain and N705 of the LRR core. Direct hydrogen-bonding interactions of BLD with S647 and Y597 via the vicinal diols of its side chain are in agreement with the earlier reports. The exact water-mediated hydrogen bond interactions have also been predicted correctly.^{9,12} These

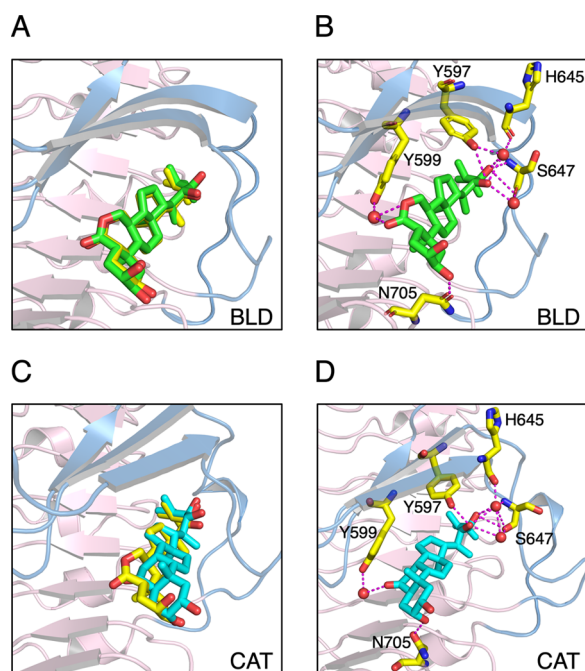


Figure 3. Simulated bound forms of (A) BLD and (C) CAT are superimposed against the BLD-bound BRI1 crystal structure. The important hydrogen-bonded interactions, both direct and water-mediated, with the residues of the island domain and LRR core of BRI1 obtained from simulations, are shown for (B) BLD and (D) CAT. BLD corresponding to the crystal structure is shown as yellow sticks, while the BLD and CAT molecules obtained from simulations are shown as green and cyan sticks, respectively.

include three water molecules, which mediate interactions between Y599 and oxygens of the B-ring lactone group, S647 and C22 hydroxyl groups, and finally among H645 and Y597, and the C22 and C23 hydroxyl groups (Figure 3B,D). In addition, N705 forms hydrogen-bonding interaction with the hydroxyl group of C3 in the A-ring (Figure 3B,D). This demonstrates the ability of MD simulations to accurately illustrate the configuration and interactions of BLD in its bound pose.

A crystal structure of CAT-bound BRI1 has yet to be solved. Thus, our simulated bound pose is the first such structure showing the spatial configuration and also the interactions of CAT with BRI1 in the bound state. We report that CAT assumes a similar but a more distorted configuration compared to BLD (Figure 3C). However, it can still interact with the same residues, which interact with BLD (Figure 3D). The slightly distorted configuration assumed by CAT is likely due to the absence of the extra oxygen in its B-ring.¹⁹ We report direct hydrogen-bonding interactions of CAT through its side-chain hydroxyl groups of C22 and C23 and its B-ring C6-attached carbonyl oxygen with Y597, S647, and N705 residues, respectively. We further report water-mediated hydrogen bond interactions involving three water molecules. They mediate interactions between the hydroxyl group of C22 and S647, carbonyl group of C6 and Y599, and finally among the hydroxyl groups of C22 and C23, and H645 and S647. Therefore, we have captured the bound pose of CAT in atomic-level detail, which provides structural insights into the lower affinity for CAT.

BLD Shows Greater Stability in the Bound Pose Than CAT. The binding dynamics of the two ligands over long time

scales was illustrated using kinetic Monte Carlo simulations on the MSM transition probability matrix. We generated 50 μ s long trajectories to show the ligand binding kinetics (Figure 4).

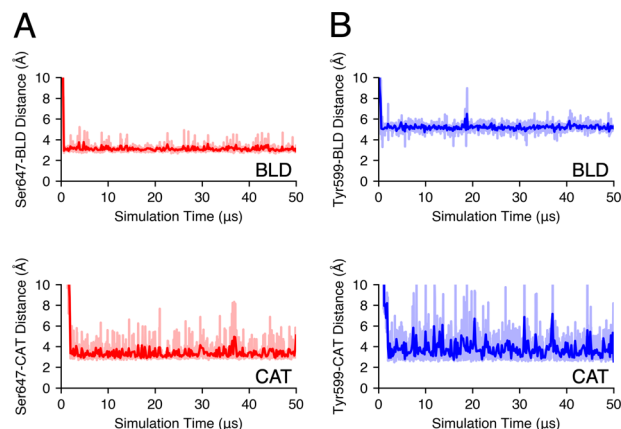


Figure 4. Kinetic Monte Carlo simulations are performed to capture the binding dynamics of both ligands over long time scales. The total simulation time is 50 μ s. (A) Distance between S647 and the side chain of either ligand is chosen to represent the binding of the ligands to the receptor and the configuration changes of the side chain upon binding. (B) Distance between Y599 and the B-ring carbonyl oxygen of either ligand is chosen to represent the spatial fluctuations of the fused A–D rings at the other end of the ligand. CAT shows a higher degree of spatial fluctuations than BLD, indicating lower stability in the bound pose.

For both the ligand systems, we selected two specific residues of BRI1, whose distances from the ligand, observed over time, could represent the binding dynamics accurately. The distance between S647 and the hydroxyl group in the side chain of each ligand was chosen to represent the binding of the ligands and also the configuration changes of the side chain upon binding (Figure 4A). The distance between Y599 and the B-ring carbonyl oxygen of the ligand was chosen to represent the spatial fluctuations of the fused rings at the other end of the ligand (Figure 4B). For both systems, the average distance of the ligand side chain from the serine residue is ~ 3 Å when bound, indicating that the ligands position themselves at similar depths inside the binding pocket of BRI1. On the other hand, the average distance of the tyrosine residue from the bound BLD is ~ 5 Å as compared to ~ 3 Å from the bound CAT. This difference results from the extra oxygen in the B-ring of BLD, which pushes the interacting carbonyl oxygen further away from the tyrosine. Our results show a higher degree of ligand fluctuations for CAT compared to that for BLD, especially highlighted by its interaction with Y599 (Figure 4B). We propose that this difference arises from the absence of the hydrogen-bonding interaction between Y599 and the nonexistent B-ring oxygen in CAT (Figure 3B,D). This results in the lower binding stability for CAT and may thus be a major reason why CAT was found to be less bioactive than BLD in previous research.^{20–23} We determined the k_{on} and k_{off} values for both the ligands, which were $1.11 \times 10^8 \text{ M}^{-1} \text{ s}^{-1}$ and $2.07 \times 10^2 \text{ s}^{-1}$ for BLD and $5.84 \times 10^7 \text{ M}^{-1} \text{ s}^{-1}$ and $4.24 \times 10^3 \text{ s}^{-1}$ for CAT. These data quantitatively suggest the slower binding and the faster unbinding for CAT compared to those for BLD. The experimental k_{on} and k_{off} for BLD were reported to be $9.49 \times 10^5 \text{ M}^{-1} \text{ s}^{-1}$ and $1.05 \times 10^{-2} \text{ s}^{-1}$, respectively, while there was no data reported for CAT. Our predicted k_{on}

for BLD is 2 orders of magnitude higher compared to experimental data, which is reasonable given that the force field for proteins is parameterized to match thermodynamic data instead of kinetic information. Previous studies have also shown that the prediction of protein–ligand binding kinetic data from MD simulations generally deviates from experimental data by 1–2 orders of magnitude.^{52,68} Our predicted k_{off} is 4 orders of magnitude larger compared to experimental data. We note that it is challenging to obtain realistic statistics on the unbinding of the ligands using unbiased MD simulations, since these inherent long time scale processes were poorly sampled in our simulations. It is beyond the scope of this study to obtain the accurate estimation of the BLD unbinding kinetics. Overall, our study reflects that BLD is more stable than CAT on BRI1 binding, primarily due to the presence of an extra oxygen in the BLD.

Transition Path Theory Reveals Similar Binding Mechanisms for BLD and CAT. To analyze the binding pathways for BLD and CAT in high resolution, we applied the transition path theory (TPT) to the MSMs and obtained the top favorable transition pathways between the ligand-unbound states and the ligand-bound states.^{64,65} For both systems, we generated the binding pathways using the MSM states where the ligands were more than 30 Å away from BRI1 as the source states, and the MSM states where the RMSDs of ligands were less than 2 Å from their respective bound poses as the sink states (Theoretical Methods). TPT can identify numerous pathways that connected through the source and the sink MSM states, along with their reactive fluxes. For example, Figure S6A,C shows the fluxes for the top 40 pathways identified using TPT for both BLD and CAT. It is clear that the flux of binding pathway becomes nearly flat after top 10 pathways. For the simplicity, we focused our analysis on the top 10 pathways and projected them onto the binding free-energy landscapes (Figure S6B,D). By inspecting the similarity between these top 10 pathways, we further lumped these pathways into two major paths for both BLD and CAT (Figures 5 and 6).

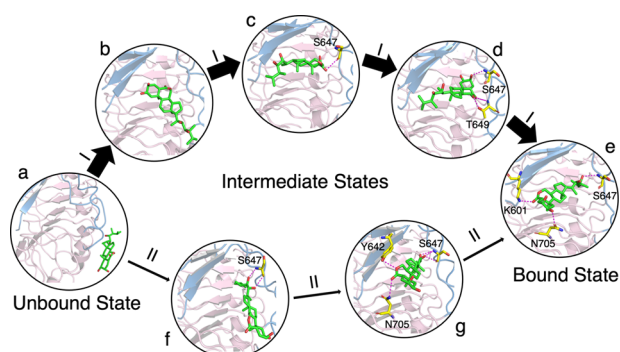


Figure 5. Top two pathways of BLD binding to BRI1 obtained using transition path theory. The unbound state is represented by (a) and the bound state by (e). Path I comprises the states (a)–(e) and outlines a binding pathway, where the A–D rings of BLD enter the BRI1 binding pocket first and then flip orientation to allow the side chain to enter the binding pocket instead, before finally assuming the bound pose. Path II comprises the states (a), (f), (g), and (e) and represents a binding pathway, where the BLD side chain leads the ligand into the binding pocket and gradually positions itself in the correct bound pose. The height of the arrows is scaled according to the relative fluxes of both pathways.

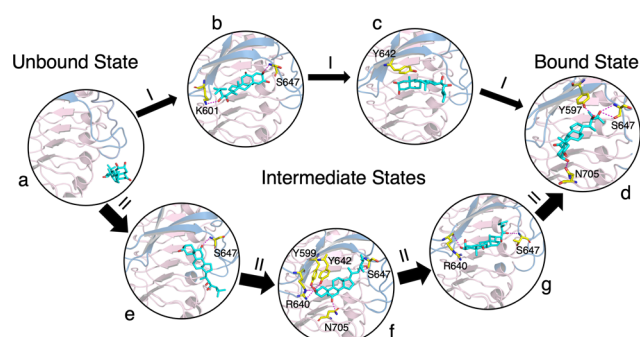


Figure 6. Top two pathways of CAT binding to BRI1 obtained using transition path theory. The unbound state is represented by (a) and the bound state by (d). Path I comprises the states (a)–(d) and outlines a binding pathway, where the A–D rings of CAT enter the BRI1 binding pocket first and then flip orientation to allow the side chain to enter the binding pocket instead, before finally assuming the bound pose. Path II comprises the states (a), (e), (f), (g), and (d) and represents a binding pathway, where the CAT side chain appears to lead the entire ligand into the binding pocket before gradually positioning itself in the correct bound pose. The height of the arrows is scaled according to the relative fluxes of both pathways.

In the first pathway for BLD binding (path I in Figure 5), BLD is observed to approach the BRI1 binding pocket with its fused A–D rings facing the binding groove. It then proceeds further into the pocket to interact with S647 of the BRI1 island domain via its hydroxyl group in the A-ring C2. Next, the hormone rings appear to move away from the binding pocket. This may represent a part of the flipping process, where BLD reverses orientation to allow its side chain to enter into the pocket and ultimately assume the bound pose. At this stage, it still maintains the previous interaction with S647 but develops new interactions with T649 via the two oxygens in its B-ring. Finally, BLD assumes its bound pose. The second binding pathway followed by BLD (path II in Figure 5) stands in contrast to the previous one in the sense that instead of the fused rings of BLD, now the side chain of the ligand leads it toward the binding pocket. In this first state, the hydroxyl groups of C22 and C23 of the side chain interact with S647, and BLD has not entered the BRI1 binding groove yet. Thereafter, BLD enters the binding pocket but is still not in its bound configuration. It continues the previous interaction with S647, meanwhile forming new interactions with Y642 and N705 through the ring oxygen and the carbonyl oxygen of its B-ring, respectively. Finally, BLD binds to the BRI1 receptor. The relative probability for path I is 92% and for path II is 8% (out of the top 10 pathways). Thus, we have captured two distinct binding pathways of BLD with BRI1, confirming the results from the free-energy landscapes.

TPT analysis further identified two favorable paths for CAT binding. The pathways captured for CAT suggest that it approaches BRI1 in a similar fashion as BLD. Both path I and path II for CAT are similar to path I in the BLD. The difference between the major two paths is whether they need to go through the nonproductive bound state (intermediate state 1 in Figure 2B). In the first pathway for CAT binding (path I in Figure 6), the fused A–D rings of CAT enter the BRI1 binding pocket first instead of the side chain. Next, hydrogen-bonding interactions are formed by the hydroxyl groups of C3 in the A-ring and C23 in the side chain with S647 and K601, respectively. Following this, the fused rings move out of the BRI1 binding pocket and form a ring–ring

hydrophobic interaction with Y642. The transition to this state resembles a similar flipping of the ring group as observed in the case of BLD. Finally, CAT enters the binding pocket and assumes its bound pose. The second pathway for CAT binding (path II in Figure 6) starts with the B-ring carbonyl oxygen forming a hydrogen bond with S647. CAT has not yet entered the binding pocket at this stage. Following this, the side chain of CAT leads it toward the binding groove. In this state, the B-ring carbonyl oxygen and the side-chain hydroxyl groups form hydrogen bonds with N705 and S647, respectively. Further, the hydroxyl group of C2 in the CAT A-ring forms a hydrogen bond with Y599, while the hydroxyl group of C3 beside it forms hydrogen bonds with R640 and Y642. Thereafter, CAT assumes a configuration where it is deeper inside the binding pocket but not yet bound. In this state, the hydroxyl groups of the A-ring C2 and the side-chain C23 form hydrogen-bonding interactions with R640 and S647, respectively. Finally, CAT positions itself perfectly to assume the bound pose. This second pathway shares some similarity to path II of BLD binding as it appears that the side chain leads the ligand into the binding pocket here as well. The relative probability for path I is 33% and for path II is 67% (out of the top 10 pathways). Overall, our results have characterized two distinct binding pathways of both BLD and CAT and have reported similarities in their binding mechanisms.

BRI1 Island Domain Undergoes a Major Conformational Restructuring Upon Ligand Binding. To quantitatively analyze the effect of ligand binding on the BRI1 island domain conformation, we calculated the root-mean-square fluctuations (RMSFs) of the C_α atoms of all BRI1 residues. The island domain was reported to undergo a major conformational change upon the binding of BLD by previous studies.^{9,12} RMSF values capture the fluctuations of the residues of a protein domain, with lower RMSF values indicating higher conformational stability. For our ligand systems, the ligand-unbound and bound states were used to calculate the fluctuations of the BRI1 residues before and after ligand binding, respectively. We further generated the free-energy landscapes for both BLD and CAT projected onto the RMSDs of the island domain and the ligand compared with their corresponding bound poses. The RMSF values of BRI1 residues and the free-energy landscape for BLD–BRI1 system are shown in Figure S7A,B and those for BRI1–CAT system are shown in Figure S7A,E respectively. A visual illustration of the protein fluctuations due to ligand binding is shown in Figure S7C,D,F,G for BLD and CAT, respectively. We report a significant reduction in RMSF values of the residues of the BRI1 island domain after BLD binding. This result is further supported by the free-energy landscape, which indicates stable bound states for deviations of the island domain less than 2 Å from the bound crystal structure. Thus, we validate previous studies, which report that BLD binding induces the island domain of BRI1 to become more ordered and fixed with respect to the LRR core.^{9,12} We further report a similar stabilization of the island domain upon CAT binding. However, the reduction in RMSF values for the island domain residues (notably residues 640–650) when CAT binds is relatively less compared to that of BLD. These results suggest that CAT induces a slightly lower degree of stabilization of the island domain, which may, in turn, increase the ligand off-binding rate. This may, thus, be another reason as to why CAT is less biologically active than BLD. Furthermore, the island domain is involved in BRI1 association with BAK1,^{9,12} and the

lower degree of stabilization of island domain may also affect the BRI1–BAK1 association. Overall, our results suggest that both BLD and CAT induce an ordering of the island domain but that this is a more prominent feature in BLD binding.

CONCLUSIONS

In this study, we utilized extensive MD simulations to provide fundamental insights into the binding mechanisms of the two most potent BRs, BLD and CAT, to the BRI1 receptor. Our results have provided a thermodynamic basis for the perception of BRs and the bioactivity difference between BLD and CAT. We have determined the standard binding free energy for the ligands, corresponding to -10.77 ± 0.11 kcal/mol for BLD and -6.9 ± 0.11 kcal/mol for CAT. The predicted ΔG° for BLD closely matches with the experimental $\Delta G^\circ_{\text{exp}}$, which is -10.92 kcal/mol.⁶⁷ Our results suggest that BLD has relatively higher binding affinity to BRI1 than CAT (~ 3.9 kcal/mol difference), in agreement with the reported bioactivity for BLD and CAT.^{20–23} We have unveiled the previously unknown bound pose for CAT, which is distorted outward the pocket compared to that for BLD, allowing for structural insights into the origin of its lower binding affinity. We propose that the lower binding affinity arises because CAT lacks an oxygen in its B-ring, which forms an important hydrogen-bonding interaction with a tyrosine residue of the BRI1 island domain. This is further supported by the predicted k_{on} and k_{off} values for both the ligands and the kinetic MC simulation results that CAT demonstrates significantly higher spatial fluctuations at the fused A–D ring side as compared to BLD. In addition, we propose that the distorted CAT-bound pose may attenuate BRI1 association with BAK1 compared to BLD, since the bound BRs directly interact with BAK1 through two hydroxyl groups in the A-ring.^{9,12} Overall, our results suggest that the absence of an oxygen in CAT may be the major reason for the lower bioactivity of CAT as compared to that of BLD.

We have identified the key intermediate states in the ligand binding pathways for both the ligands. We report two distinct pathways for both the ligands. The difference in these two pathways lies in the way the hormones approach the BRI1 binding pocket. We report that either the linked A–D rings of the ligands enter the binding pocket first and later flip orientation to allow the side chain to enter the pocket, or the side chain enters the binding pocket first and then the ligands gradually fix themselves in their final bound poses. We have further captured the BRI1 residues interacting with the two ligands during binding. These residues are a part of either the island domain or the surrounding LRR core, thus confirming the hypothesized importance of these BRI1 regions in BR binding.^{9,12} Thus, we have characterized the binding pathways followed by BLD and CAT in atomistic detail, which provides structural insights into the binding process of BRs. We report a nonproductive binding pose for both BLD and CAT and reveal that this pose is more stable for the latter. It is likely that this intermediate state hinders both ligands from assuming the correct bound pose, thereby lowering the affinity by decreasing the ligand on-binding rates. Since the nonproductive binding pose for CAT is ~ 3 kcal/mol more stable as compared to that for BLD, it may further contribute to the lower bioactivity of CAT. Interestingly, similar nonproductive binding poses are observed for the binding of plant hormone abscisic acid to both PYL5 and PYL10 receptors in *A. thaliana*.³⁶ Overall, the discovery of nonproductive binding poses may provide some

guidance on future agrochemical discovery to design ligands with enhanced affinities for targeting these plant receptors.

Our results have also confirmed the hypotheses that the island domain undergoes a major structural restructuring upon ligand binding.^{9,12} We report a significant reduction in RMSF values for the island domain residues upon the binding of BRs. These results indicate that the binding of BRs stabilizes the island domain in general. However, we observed that CAT binding results in a smaller reduction in RMSF values of the island domain compared to BLD. Since the island domain is directly involved in interaction with both BRs and BAK1,^{9,12} we thus propose that the reduced conformational restructuring of the island domain on CAT binding might be an additional reason for the lower bioactivity of CAT compared to that of BLD.

In conclusion, our study provides critical molecular insights into the perception of the two most potent BRs, BLD and CAT, by BRI1. Our results probing the differences in binding of the two ligands as a result of their structural dissimilarities may help future research on BR perception in plant cells and agrochemical discovery of more bioactive BR analogs. Finally, the leucine-rich repeat receptor-like kinases in plants play a vital role in the perception of various plant peptides and further modulate plant growth, development, and stress responses.^{69,70} Exporting the computational methods used in this study to gain detailed atomistic pictures of the binding of plant peptides and other phytohormones, to their respective receptors, might lead to a better understanding of plant signaling mechanism.

■ ASSOCIATED CONTENT

● Supporting Information

The Supporting Information is available free of charge at <https://pubs.acs.org/doi/10.1021/acs.jpcb.9b09377>.

Convergence of implied time scales with respect to lag time; GMRQ scores for MSM hyperparameter selection; PMFs for BLD binding to BRI1 projected onto Euclidean coordinates; PMFs for CAT binding to BRI1 projected onto Euclidean coordinates; error bars for the free-energy landscapes; flux analysis of binding pathways identified from TPT; RMSF analysis of the island domain in BRI1; summary of MD simulations of BLD binding to BRI1; summary of MD simulations of CAT binding to BRI1; featurization metrics used for analyzing the BRI1–BLD simulation datasets; and featurization metrics used for analyzing the BRI1–CAT simulation datasets (PDF)

■ AUTHOR INFORMATION

Corresponding Author

*E-mail: diwakar@illinois.edu

ORCID

Chuankai Zhao: 0000-0002-6879-6514

Alexander S. Moffett: 0000-0003-1631-2722

Diwakar Shukla: 0000-0003-4079-5381

Author Contributions

○F.A. and A.D. contributed equally to this work.

Notes

The authors declare no competing financial interest.

■ ACKNOWLEDGMENTS

The authors acknowledge the support from the Blue Waters sustained-petascale computing project, which is funded by the National Science Foundation (awards OCI-0725070 and ACI-1238993) and the state of Illinois. F.A. acknowledges the support by the Blue Waters Student Internship Program funded by the Shodor Education Foundation. A.D. acknowledges the support by the Khorana Program for Scholars funded by the Department of Biotechnology, Government of India. D.S. acknowledges the support from the Foundation for Food and Agriculture Research via the New Innovator Award in Food & Agriculture Research.

■ REFERENCES

- (1) Belkhadir, Y.; Jaillais, Y. The Molecular Circuitry of Brassinosteroid Signaling. *New Phytol.* **2015**, *206*, 522–540.
- (2) Vert, G.; Chory, J. Crosstalk in Cellular Signaling: Background Noise or the Real Thing. *Dev. Cell* **2011**, *21*, 985–991.
- (3) Moreno-Castillo, E.; Ramírez-Echemendía, D. P.; Hernández-Campoalegre, G.; Mesa-Tejeda, D.; Coll-Manchado, F.; Coll-García, Y. In Silico Identification of New Potentially Active Brassinosteroid Analogues. *Steroids* **2018**, *138*, 35–42.
- (4) Zhu, J.-Y.; Sae-Seaw, J.; Wang, Z.-Y. Brassinosteroid Signalling. *Development* **2013**, *140*, 1615–1620.
- (5) Lei, B.; Liu, J.; Yao, X. Unveiling the Molecular Mechanism of Brassinosteroids: Insights From Structure-Based Molecular Modeling Studies. *Steroids* **2015**, *104*, 111–117.
- (6) Han, Z.; Sun, Y.; Chai, J. Structural Insight Into the Activation of Plant Receptor Kinases. *Curr. Opin. Plant Biol.* **2014**, *20*, 55–63.
- (7) Sun, Y.; Han, Z.; Tang, J.; Hu, Z.; Chai, C.; Zhou, B.; Chai, J. Structure Reveals That BAK1 as a Co-Receptor Recognizes the BRI1-Bound Brassinolide. *Cell Res.* **2013**, *23*, 1326–1329.
- (8) Wang, Z.-Y.; Seto, H.; Fujioka, S.; Yoshida, S.; Chory, J.; Is, B. R. I. A Critical Component of a Plasma-Membrane Receptor for Plant Steroids. *Nature* **2001**, *410*, 380–383.
- (9) She, J.; Han, Z.; Kim, T.-W.; Wang, J.; Cheng, W.; Chang, J.; Shi, S.; Wang, J.; Yang, M.; Wang, Z.-Y.; Chai, J. Structural Insight Into Brassinosteroid Perception by BRI1. *Nature* **2011**, *474*, 472–476.
- (10) Li, J.; Chory, J. A Putative Leucine-Rich Repeat Receptor Kinase Involved in Brassinosteroid Signal Transduction. *Cell* **1997**, *90*, 929–938.
- (11) Friedrichsen, D. M.; Joazeiro, C. A.; Li, J.; Hunter, T.; Chory, J. Brassinosteroid-Insensitive-1 Is a Ubiquitously Expressed Leucine-Rich Repeat Receptor Serine/Threonine Kinase. *Plant Physiol.* **2000**, *123*, 1247–1256.
- (12) Hothorn, M.; Belkhadir, Y.; Dreux, M.; Dabi, T.; Noel, J. P.; Wilson, I. A.; Chory, J. Structural Basis of Steroid Hormone Perception by the Receptor Kinase BRI1. *Nature* **2011**, *474*, 467–471.
- (13) Shang, Y.; Lee, M.; Li, J.; Nam, K. Characterization of cp3 Reveals a New bri1 Allele, bri1-120, and the Importance of the LRR Domain of BRI1 Mediating BR Signaling. *BMC Plant Biol.* **2011**, *11*, 8.
- (14) Sakurai, A.; Fujioka, S. The Current Status of Physiology and Biochemistry of Brassinosteroids. *Plant Growth Regul.* **1993**, *13*, 147–159.
- (15) Bajguz, A.; Tretyn, A. The Chemical Characteristic and Distribution of Brassinosteroids in Plants. *Phytochemistry* **2003**, *62*, 1027–1046.
- (16) Noguchi, T.; Fujioka, S.; Choe, S.; Takatsuto, S.; Tax, F. E.; Yoshida, S.; Feldmann, K. A. Biosynthetic Pathways of Brassinolide in Arabidopsis. *Plant Physiol.* **2000**, *124*, 201–210.
- (17) Grove, M. D.; Spencer, G. F.; Rohwedder, W. K.; Mandava, N.; Worley, J. F.; Warthen, J. D.; Steffens, G. L.; Flippen-Anderson, J. L.; Cook, J. C. Brassinolide, a Plant Growth-Promoting Steroid Isolated From Brassica Napus Pollen. *Nature* **1979**, *281*, 216–217.

- (18) Suzuki, H.; Fujioka, S.; Takatsuto, S.; Yokota, T.; Murofushi, N.; Sakurai, A. Biosynthesis of Brassinolide From Castasterone in Cultured Cells of *Catharanthus Roseus*. *J. Plant Growth Regul.* **1993**, *12*, 101–106.
- (19) Yokota, T.; Arima, M.; Takahashi, N. Castasterone, a New Phytosterol With Plant-Hormone Potency, From Chestnut Insect Gall. *Tetrahedron Lett.* **1982**, *23*, 1275–1278.
- (20) Fujioka, S.; Inoue, T.; Takatsuto, S.; Yanagisawa, T.; Yokota, T.; Sakurai, A. Biological Activities of Biosynthetically-related Congeners of Brassinolide. *Biosci. Biotechnol. Biochem.* **1995**, *59*, 1973–1975.
- (21) Fujioka, S.; Noguchi, T.; Takatsuto, S.; Yoshida, S. Activity of Brassinosteroids in the Dwarf Rice Lamina Inclination Bioassay. *Phytochemistry* **1998**, *49*, 1841–1848.
- (22) Suzuki, H.; Kim, S.; Takahashi, N.; Yokota, T. Metabolism of Castasterone and Brassinolide in Mung Bean Explant. *Phytochemistry* **1993**, *33*, 1361–1367.
- (23) Thompson, M. J.; Meudt, W. J.; Mandava, N.; Dutky, S. R.; Lusby, W. R.; Spaulding, D. W. Synthesis of Brassinosteroids and Relationship of Structure to Plant Growth-Promoting Effects. *Steroids* **1982**, *39*, 89–105.
- (24) Casalino, L.; Palermo, G.; Spinello, A.; Rothlisberger, U.; Magistrato, A. All-Atom Simulations Disentangle the Functional Dynamics Underlying Gene Maturation in the Intron Lariat Spliceosome. *Proc. Natl. Acad. Sci. U.S.A.* **2018**, *115*, 6584–6589.
- (25) Casalino, L.; Palermo, G.; Rothlisberger, U.; Magistrato, A. Who Activates the Nucleophile in Ribozyme Catalysis? An Answer from the Splicing Mechanism of Group II Introns. *J. Am. Chem. Soc.* **2016**, *138*, 10374–10377.
- (26) Palermo, G.; Casalino, L.; Magistrato, A.; McCammon, J. A. Understanding the Mechanistic Basis of Non-Coding RNA Through Molecular Dynamics Simulations. *J. Struct. Biol.* **2019**, *206*, 267–279.
- (27) Hollingsworth, S. A.; Dror, R. O. Molecular Dynamics Simulation for All. *Neuron* **2018**, *99*, 1129–1143.
- (28) Karplus, M.; McCammon, J. A. Molecular Dynamics Simulations of Biomolecules. *Nat. Struct. Mol. Biol.* **2002**, *9*, 646–652.
- (29) Bowman, G. R.; Ensign, D. L.; Pande, V. S. Enhanced Modeling via Network Theory: Adaptive Sampling of Markov State Models. *J. Chem. Theory Comput.* **2010**, *6*, 787–794.
- (30) Shamsi, Z.; Moffett, A. S.; Shukla, D. Enhanced Unbiased Sampling of Protein Dynamics Using Evolutionary Coupling Information. *Sci. Rep.* **2017**, *7*, No. 12700.
- (31) Shamsi, Z.; Cheng, K. J.; Shukla, D. Reinforcement Learning Based Adaptive Sampling: REAPing Rewards by Exploring Protein Conformational Landscapes. *J. Phys. Chem. B* **2018**, *122*, 8386–8395.
- (32) Zhao, C.; Shukla, D. SAXS-guided Enhanced Unbiased Sampling for Structure Determination of Proteins and Complexes. *Sci. Rep.* **2018**, *8*, No. 17748.
- (33) Chodera, J. D.; Noé, F. Markov State Models of Biomolecular Conformational Dynamics. *Curr. Opin. Struct. Biol.* **2014**, *25*, 135–144.
- (34) Shukla, D.; Hernández, C. X.; Weber, J. K.; Pande, V. S. Markov State Models Provide Insights into Dynamic Modulation of Protein Function. *Acc. Chem. Res.* **2015**, *48*, 414–422.
- (35) Husic, B. E.; Pande, V. S. Markov State Models: From an Art to a Science. *J. Am. Chem. Soc.* **2018**, *140*, 2386–2396.
- (36) Shukla, S.; Zhao, C.; Shukla, D. Dewetting Controls Plant Hormone Perception and Initiation of Drought Resistance Signaling. *Structure* **2019**, *27*, 692–702.
- (37) Selvam, B.; Shamsi, Z.; Shukla, D. Universality of the Sodium Ion Binding Mechanism in Class A G-Protein-Coupled Receptors. *Angew. Chem., Int. Ed.* **2018**, *57*, 3048–3053.
- (38) Moffett, A. S.; Bender, K. W.; Huber, S. C.; Shukla, D. Allosteric Control of a Plant Receptor Kinase through S-Glutathionylation. *Biophys. J.* **2017**, *113*, 2354–2363.
- (39) Moffett, A. S.; Bender, K. W.; Huber, S. C.; Shukla, D. Molecular Dynamics Simulations Reveal the Conformational Dynamics of *Arabidopsis thaliana* BRI1 and BAK1 Receptor-Like Kinases. *J. Biol. Chem.* **2017**, *292*, 12643–12652.
- (40) Selvam, B.; Mittal, S.; Shukla, D. Free Energy Landscape of the Complete Transport Cycle in a Key Bacterial Transporter. *ACS Cent. Sci.* **2018**, *4*, 1146–1154.
- (41) Selvam, B.; Yu, Y.-C.; Chen, L.-Q.; Shukla, D. Molecular Basis of the Glucose Transport Mechanism in Plants. *ACS Cent. Sci.* **2019**, *5*, 1085–1096.
- (42) Humphrey, W.; Dalke, A.; Schulten, K. VMD: Visual Molecular Dynamics. *J. Mol. Graphics* **1996**, *14*, 33–38.
- (43) Eastman, P.; et al. OpenMM 4: A Reusable, Extensible, Hardware Independent Library for High Performance Molecular Simulation. *J. Chem. Theory Comput.* **2013**, *9*, 461–469.
- (44) Anandakrishnan, R.; Aguilar, B.; Onufriev, A. V. H++ 3.0: Automating pK Prediction and the Preparation of Biomolecular Structures for Atomistic Molecular Modeling and Simulations. *Nucleic Acids Res.* **2012**, *40*, W537–W541.
- (45) Maier, J. A.; Martinez, C.; Kasavajhala, K.; Wickstrom, L.; Hauser, K. E.; Simmerling, C. ff14SB: Improving the Accuracy of Protein Side Chain and Backbone Parameters From ff99SB. *J. Chem. Theory Comput.* **2015**, *11*, 3696–3713.
- (46) Wang, J.; Wolf, R. M.; Caldwell, J. W.; Kollman, P. A.; Case, D. A. Development and Testing of a General Amber Force Field. *J. Comput. Chem.* **2004**, *25*, 1157–1174.
- (47) Case, D. A. et al. *Amber 18*; University of California: San Francisco, CA, 2018.
- (48) Loncharich, R. J.; Brooks, B. R.; Pastor, R. W. Langevin Dynamics of Peptides: The Frictional Dependence of Isomerization Rates of N-Acetylalanine-N'-Methylamide. *Biopolymers* **1992**, *32*, 523–535.
- (49) Berendsen, H. J.; Postma, J.; van Gunsteren, W. F.; DiNola, A.; Haak, J. Molecular Dynamics With Coupling to an External Bath. *J. Chem. Phys.* **1984**, *81*, 3684–3690.
- (50) Darden, T.; York, D.; Pedersen, L. Particle Mesh Ewald: An Nlog(N) Method for Ewald Sums in Large Systems. *J. Chem. Phys.* **1993**, *98*, 10089–10092.
- (51) Ryckaert, J.-P.; Ciccotti, G.; Berendsen, H. J. Numerical Integration of the Cartesian Equations of Motion of a System With Constraints: Molecular Dynamics of N-Alkanes. *J. Comput. Phys.* **1977**, *23*, 327–341.
- (52) Buch, I.; Giorgino, T.; Fabritiis, G. D. Complete Reconstruction of an Enzyme-Inhibitor Binding Process by Molecular Dynamics Simulations. *Proc. Natl. Acad. Sci. U.S.A.* **2011**, *108*, 10184–10189.
- (53) Lawrenz, M.; Shukla, D.; Pande, V. S. Cloud Computing Approaches for Prediction of Ligand Binding Poses and Pathways. *Sci. Rep.* **2015**, *5*, No. 7918.
- (54) Mendes, C. L.; Bode, B.; Bauer, G. H.; Enos, J.; Beldica, C.; Kramer, W. T. Deploying a Large Petascale System: The Blue Waters Experience. *Procedia Comput. Sci.* **2014**, *29*, 198–209.
- (55) Pande, V. S.; Beauchamp, K.; Bowman, G. R. Everything You Wanted to Know About Markov State Models but Were Afraid to Ask. *Methods* **2010**, *52*, 99–105.
- (56) McGibbon, R. T.; Beauchamp, K. A.; Harrigan, M. P.; Klein, C.; Swails, J. M.; Hernández, C. X.; Schwantes, C. R.; Wang, L.-P.; Lane, T. J.; Pande, V. S. MDTraj: A Modern Open Library for the Analysis of Molecular Dynamics Trajectories. *Biophys. J.* **2015**, *109*, 1528–1532.
- (57) Naritomi, Y.; Fuchigami, S. Slow Dynamics in Protein Fluctuations Revealed by Time-Structure Based Independent Component Analysis: The Case of Domain Motions. *J. Chem. Phys.* **2011**, *134*, No. 065101.
- (58) McGibbon, R. T.; Pande, V. S. Variational Cross-Validation of Slow Dynamical Modes in Molecular Kinetics. *J. Chem. Phys.* **2015**, *142*, 124105.
- (59) Harrigan, M. P.; Sultan, M. M.; Hernández, C. X.; Husic, B. E.; Eastman, P.; Schwantes, C. R.; Beauchamp, K. A.; McGibbon, R. T.; Pande, V. S. MSMBuilder: Statistical Models for Biomolecular Dynamics. *Biophys. J.* **2017**, *112*, 10–15.
- (60) McGibbon, R. T.; Hernández, C. X.; Harrigan, M. P.; Kearnes, S.; Sultan, M. M.; Jastrzebski, S.; Husic, B. E.; Pande, V. S. Osprey:

Hyperparameter Optimization for Machine Learning. *J. Open Source Software* **2016**, *1*, 34.

(61) Hunter, J. D. Matplotlib: A 2D Graphics Environment. *Comput. Sci. Eng.* **2007**, *9*, 90–95.

(62) Doudou, S.; Burton, N. A.; Henchman, R. H. Standard Free Energy of Binding from a One-Dimensional Potential of Mean Force. *J. Chem. Theory Comput.* **2009**, *5*, 909–918.

(63) Metzner, P.; Noé, F.; Schütte, C. Estimating the Sampling Error: Distribution of Transition Matrices and Functions of Transition Matrices for Given Trajectory Data. *Phys. Rev. E* **2009**, *80*, 021106.

(64) E, W.; Vanden-Eijnden, E. Towards a Theory of Transition Paths. *J. Stat. Phys.* **2006**, *123*, 503.

(65) E, W.; Vanden-Eijnden, E. Transition-Path Theory and Path-Finding Algorithms for the Study of Rare Events. *Annu. Rev. Phys. Chem.* **2010**, *61*, 391–420.

(66) Roe, D. R.; Cheatham, T. E. PTRAJ and CPPTRAJ: Software for Processing and Analysis of Molecular Dynamics Trajectory Data. *J. Chem. Theory Comput.* **2013**, *9*, 3084–3095.

(67) Hohmann, U.; Santiago, J.; Nicolet, J.; Olsson, V.; Spiga, F. M.; Hothorn, L. A.; Butenko, M. A.; Hothorn, M. Mechanistic Basis for the Activation of Plant Membrane Receptor Kinases by SERK-Family Coreceptors. *Proc. Natl. Acad. Sci. U.S.A.* **2018**, *115*, 3488–3493.

(68) Plattner, N.; Noé, F. Protein Conformational Plasticity and Complex Ligand-Binding Kinetics Explored by Atomistic Simulations and Markov Models. *Nat. Commun.* **2015**, *6*, No. 7653.

(69) Hohmann, U.; Lau, K.; Hothorn, M. The Structural Basis of Ligand Perception and Signal Activation by Receptor Kinases. *Annu. Rev. Plant Biol.* **2017**, *68*, 109–137.

(70) Zhang, H.; Han, Z.; Song, W.; Chai, J. Structural Insight into Recognition of Plant Peptide Hormones by Receptors. *Mol. Plant* **2016**, *9*, 1454–1463.